J Mater Sci: Mater Electron (2017) 28:7692–7707
DOI 10.1007/s10854-017-6463-z

Composition dependence of the multifunctional properties of Nd-doped $Bi_4Ti_3O_{12}$ ceramics

Sergey A. Ivanov[1,2] · Tapati Sarkar[1] · Elena A. Fortalnova[3] · Ekaterina D. Politova[2] · Sergey Yu. Stefanovich[2] · Marina G. Safronenko[3] · Per Nordblad[1] · Roland Mathieu[1]

Received: 25 November 2016 / Accepted: 25 January 2017 / Published online: 15 February 2017

Abstract Sample preparation, evolution of the crystal structure with Nd content at room temperature, as well as dielectric and magnetic properties of polycrystalline $Bi_{4-x}Nd_xTi_3O_{12}$ solid solutions (x = 0.0, 0.5, 1.0, 1.5, and 2.0) are reported. These solid solutions were structurally characterized by X-ray powder diffraction using Rietveld refinements. For $x \leq 1.0$, the samples crystallize in an orthorhombic symmetry. The structural data could be refined using the polar orthorhombic space group *B*2*cb*. The orthorhombicity decreases with increasing Nd^{3+} concentration, and a paraelectric tetragonal structure (space group *I*4/*mmm*) is stabilized for $x > 1$.The ferroelectric Curie temperature was found to monotonously decrease with increasing Nd concentration. A polar-to-nonpolar phase transition takes place near x = 1, reflecting the existence of a morphotropic phase boundary between $1.0 < x < 1.5$ at room temperature. All samples were found to be paramagnetic down to 5 K, however, the presence of significant antiferromagnetic interaction is inferred from Curie–Weiss analyses of the temperature dependence of the magnetic susceptibility of the doped samples. The effect of Nd^{3+} substitution on structure–property relationship is discussed and compared to that of other lanthanide cations.

✉ Roland Mathieu
roland.mathieu@angstrom.uu.se

[1] Department of Engineering Sciences, Uppsala University, Box 534, 75121 Uppsala, Sweden

[2] Karpov Institute of Physical Chemistry, ul. Vorontsovo Pole, 10, 105064 Moscow, Russia

[3] RUDN University, ul. Miklukho-Maklaya 6, Moscow 117198, Russia

1 Introduction

The search and design of new multiferroic compounds possessing electric dipole moment and magnetic ordering in a single phase is currently a prioritized direction of research in the field of materials science [1–4]. The interest largely arises from the possibility of cross-controlling magnetic field/electric field and polarization/magnetization, that could provide a route to advanced memory devices [5, 6]. During the last decades, the main efforts in this research field have been focused on different perovskite compounds [4] whereas other structure types have been less studied [7]. However, in recent years bismuth layer-structured ferroelectrics have attracted much attention because of their high ferroelectric Curie temperature (T_c), large spontaneous polarization, and their possible applications as lead-free components in electronic functional devices [8, 9]. For instance, the compound $Bi_4Ti_3O_{12}$ (BTO) undergoes a first-order ferroelectric transition at $T_C = 676\,°C$ [8]. Unfortunately, pure $Bi_4Ti_3O_{12}$ suffers from high leakage electric currents, poor fatigue endurance, and small remnant polarization [10]. On the other hand, Nd-substituted $Bi_4Ti_3O_{12}$ ($Bi_{4-x}Nd_xTi_3O_{12}$ (BNTO)) has received a great deal of attention since this substitution e.g. significantly enlarges the remnant polarization compared to that of the pure compound [11–14].

$Bi_4Ti_3O_{12}$ belongs to the Aurivillius structure family, which can be described as a regular stacking of fluorite-like $[Bi_2O_2]^{2+}$ slabs and perovskite-like blocks $[A_{n-1}B_nO_{3n+1}]^{2-}$ ($\boldsymbol{n} = 3$), where the integer, $\boldsymbol{n}$, describes the number of sheets of corner-sharing BO_6 octahedra forming the ABO_3-type perovskite blocks [15–18] (cf. Fig. 1). The electronic configuration of the Bi^{3+} cation is [Xe]4f $^{14}5d^{10}6s^2$, where the $6s^2$ lone pair is responsible for the high polarizability of this cation and its stereochemical activity.

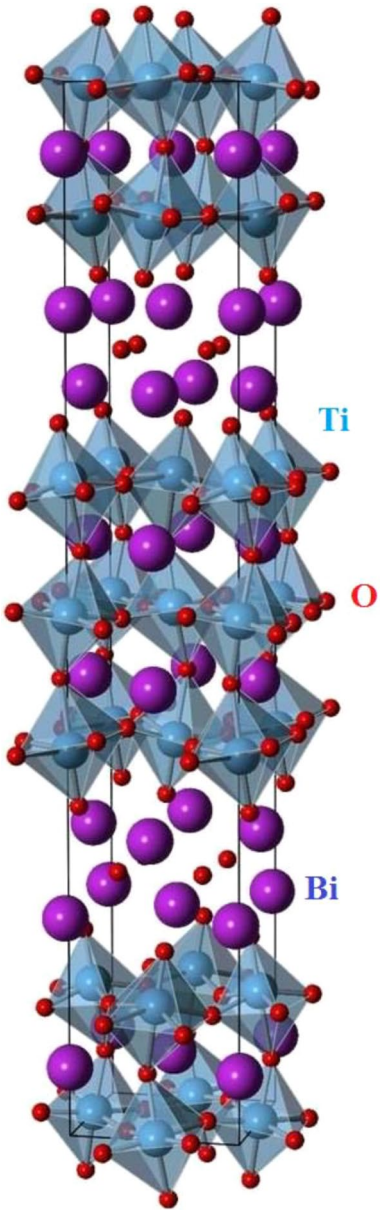

Fig. 1 Crystal structure of $Bi_4Ti_3O_{12}$; drawn using VESTA [54]

The Aurivillius family constitutes a class of compounds where new multiferroics with good ferroelectric and magnetic properties may be found [19–21]. As mentioned, $Bi_4Ti_3O_{12}$ has well-established high temperature ferroelectric properties [22, 23], that can be enhanced by the substitution of Bi by Nd causing enlarged remnant polarization [24–26] accompanied by other changes of structural and physical properties [27–31]. Recently, there have been several investigations on the effects of doping $Bi_4Ti_3O_{12}$ by various magnetic species [32–38]. However, these materials do not acquire magnetic long range order even at low temperatures.

Here we report the synthesis and systematic physicochemical investigations of the dielectric and magnetic properties of the $Bi_{4-x}Nd_xTi_3O_{12}$ series within a wide concentration range, $0 \le x \le 2$.

2 Experimental

2.1 Sample preparation

Solid solution ceramics of $Bi_{4-x}Nd_xTi_3O_{12}$ with $0 \le x \le 2$ were synthesized via conventional solid state reaction technique using stoichiometric quantities of Bi_2O_3 (99.9%), Nd_2O_3 (99.9%), and TiO_2 (99.9%). All the oxides were calcined before use to remove adsorbed water and carbon dioxide. The synthesis occurred following the equation: $(4-x)/2Bi_2O_3 + 3TiO_2 + x/2Nd_2O_3 \rightarrow Bi_{4-x}Nd_xTi_3O_{12}$. Stoichiometric quantities of the initial reagents were homogenized with ethanol in an agate mortar and pressed into pellets. Next, the samples were successively annealed at $T_1 = 973$ K, $T_2 = 1073$ K, and $T_3 = 1173$ K (10 h at each temperature) with intermediate regrinding in ethanol. The heating rate was 10 K/min for each stage of the synthesis. The samples with high Nd_2O_3 content ($x = 1.5$ and 2.0) were additionally heated at $T_4 = 1273$ K (10 h) for complete phase formation.

2.2 X-ray powder diffraction

The phase purity of the powder samples were checked using X-ray powder diffraction (XRPD) patterns obtained with a D-5000 diffractometer using CuK_α radiation. The ceramic samples of BNTO were crushed into powder in an agate mortar and suspended in ethanol. A Si substrate was covered with several drops of the resulting suspension, leaving randomly oriented crystallites after drying. The XRPD data for Rietveld analysis were collected at room temperature on a Bruker D8 Advance diffractometer (solid state rapid LynxEye detector, Ge monochromatized Cu $K_{\alpha 1}$ radiation, Bragg–Brentano geometry, DIFFRACT plus software) in the 2θ range 10°–152° with a step size of 0.02° (counting time was 15 s per step). The slit system was selected to ensure that the X-ray beam was completely focused within the sample for all 2θ angles. The XRPD experimental diffraction patterns were analyzed via the Rietveld profile method using the FULLPROF program [39]. The diffraction peaks were described by a pseudo-Voigt profile function with a Lorentzian contribution to the Gaussian peak shape. A peak asymmetry correction was made for angles below 35° (2θ). Background intensities were described by a polynomial with six coefficients. During the refinements, the two A-type cations (Bi and Nd) were allowed to occupy all possible metal sites. The IVTON software [40] was

employed to characterize the spatial coordination of the A and B-site cations and to obtain bond lengths, volumes of coordination polyhedral, and cation displacements from the center of polyhedra.

2.3 Thermal analysis

The phase interactions at each stage of the synthesis were investigated via thermogravimetric analysis (DTA/TG) using an SDT Q600 thermoanalyzer (Pt–Pt/Rh thermocouple) in the temperature range of 273–1523 K in air. Heating rates of $\upsilon = 5$ and 10 K/min were used and the temperature measurement accuracy was $\Delta T = \pm 1°$. The accuracy of the thermogravimetric measurements was $\Delta m/m = 0.5\%$.

2.4 Chemical composition

The average cation composition of the synthesized ceramics was estimated by EDS analysis using Epsilon1 microanalyzer (PanAnalytical). The chemical composition of the powder samples for structural investigations was analyzed by energy-dispersive spectroscopy (EDS) using a JEOL 840A scanning electron microscope and INCA 4.07 (Oxford Instruments) software.

2.5 Second harmonic generation (SHG) measurements

The samples were characterized via SHG measurements in reflection geometry, using a pulsed Nd:YAG laser ($\lambda = 1.064$ μm). The tests were performed in the temperature range of 25–700 °C. The SHG signal $I_2\omega$ was measured from the polycrystalline samples relative to α-quartz standard at room temperature in the Q-switching mode with a repetition rate of 4 Hz. To make relevant comparisons, the BNTO microcrystalline powders and α-quartz standard were sieved into the same particle size range since the SHG signal is known to depend strongly on the particle size [41].

2.6 IR spectroscopy

The IR-Fourier analysis of the $Bi_{4-x}Nd_xTi_3O_{12}$ samples was performed in the frequency range of $\nu = 400$–1500 cm^{-1} using the spectrophotometer FSM-1202 in continuous mode. The samples were pressed into pellets with KBr in the ratio 1:100.

2.7 Magnetic and dielectric measurements

Magnetization measurements were performed using a superconducting quantum interference device magnetometer (SQUID) from Quantum Design. The temperature dependence of the magnetization was recorded under different magnetic fields using zero-field-cooled (ZFC) and field-cooled (FC) protocols. Magnetic hysteresis loops were recorded at low temperature ($T = 5$ K).

Dielectric properties of BNTO ceramic samples were measured using ceramic disks (0.3 mm thick) with silver electrodes fired on both sides. The dielectric constant and loss tangent were derived from an impedance analyzer HP 4284A Agilent 4284A Precision LCR Meter in the range of frequencies 10^2–10^6 Hz (1 V) and temperatures 298–1023 K. To determine T_C, capacitance measurements were performed as a function of temperature in an automated temperature controlled furnace interfaced with a computer for data acquisition.

3 Results

3.1 Sample characterization

EDS measurements revealed the presence of all the cations in the BNTO samples. According to the elemental analysis done on 20 different crystallites of each sample, the metal compositions of the BNTO ceramics are close to expected values. Scanning electron micrographs showed practically uniform distribution of grains of average size ranging between 1.3 and 1.8 μm. The average grain size decreased with an increase in the Nd concentration. The oxygen content, determined using iodometric titration, was found to vary between 11.98(3) and 12.01(3) for the different samples without any correlation between the oxygen content and Nd concentration. All these values are very close to the expected values. Thus, we can conclude that the compositions of the samples were close to the nominal ones.

3.2 SHG measurements

Being a sensitive and reliable technique for establishing the presence or absence of acentric distortions, the SHG technique was used as a test for center of symmetry in the synthesized samples. Powder SHG measurements on $Bi_4Ti_3O_{12}$ indicated that the material has an SHG signal of approximately 200 times that of α-SiO_2 standard at room temperature. As the amount of Nd^{3+} cation in $Bi_{4-x}Nd_xTi_3O_{12}$ increases to $x = 0.5$ and 1, the SHG signals decrease to 75 and 40 times that of α-SiO_2, respectively, as illustrated in Fig. 2c. However, negligible SHG signal was recorded for samples with $x > 1.0$, suggesting that these BNTO samples are centrosymmetric.

Figure 2a shows an abrupt loss of the SHG signal with temperature near 660 °C for the undoped sample ($x = 0$), reflecting the phase transition to a centrosymmetric phase at that temperature (i.e. Tc ~ 660 °C). For the compound with $x = 1$, a step-like change of $I_{2w}(T)$ with thermal hysteresis is also observed, albeit less sharp than what is observed for

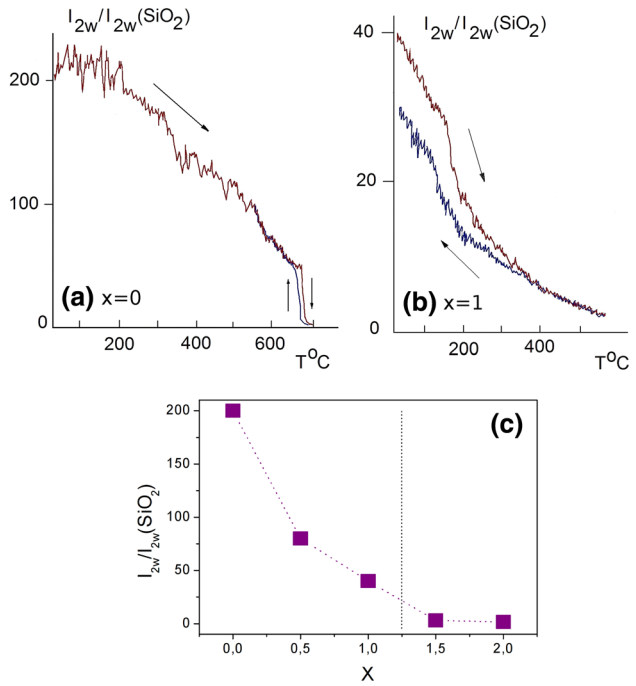

Fig. 2 Temperature dependence of the SHG signal for $Bi_{4-x}Nd_xTi_4O_{12}$ with **a** x = 0 and **b** x = 1 during heating and cooling. **c** Concentration dependence of the SHG signal for $Bi_{4-x}Nd_xTi_3O_{12}$

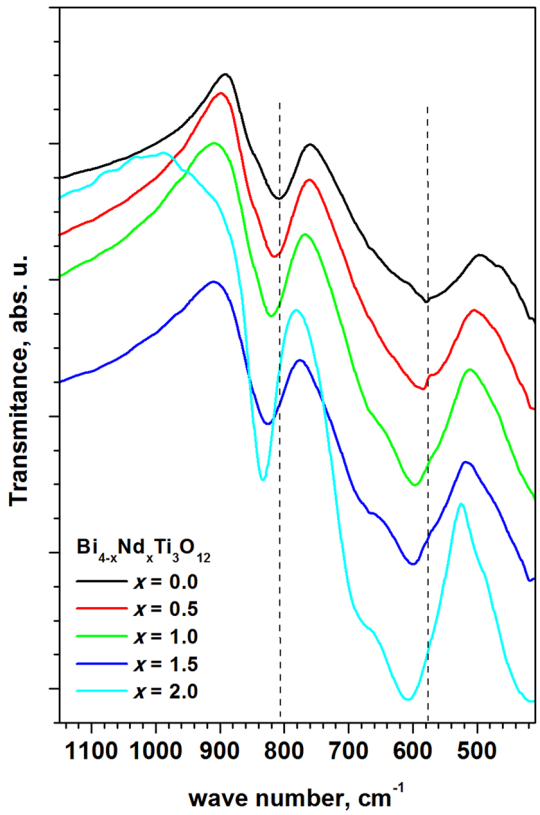

Fig. 3 IR spectra of $Bi_{4-x}Nd_xTi_3O_{12}$

the undoped compound, and at a lower temperature, near 200 °C (see Fig. 2b). Above this temperature a two-phase region exists, where a residue of a noncentrosymmetric ferroelectric phase coexists with fragments of a paraelectric phase. As a result the SHG signal gradually decreases up to higher temperatures.

3.3 IR spectroscopy

The IR spectra of the BNTO samples (Fig. 3) were in good agreement with previously reported data [33]. The presence of two wide bands in the range of ~870–800 and ~740–530 cm^{-1} in the spectra are due to the vibrations of Ti–O bonds in the TiO_6 octahedra. The maxima of these bands shift to higher frequencies with an increase in x. The observed shifts can be explained by different factors [33, 42]: a decrease in the length and therefore an increase in the energy of the Ti–O bonds, the displacement of the TiO_6 octahedra along the *a* axis and the change of the Ti–O valence bond angle. Bi^{3+} ($6s^2$) and Nd^{3+} ($4f^3$) have different ionic radii (1.17 and 1.109 Å for CN = 8, respectively) [43]. As a result, the unit cell volume and Ti–O bond lengths decrease with an increase in the Nd^{3+} concentration.

The occurrence of a shoulder at ~680–660 cm^{-1} on the side of the absorption band in the range ~740–530 cm^{-1} for x = 1.0 and its strengthening with an increase in x may be related to approaching the concentration for which an orthorhombic to tetragonal phase transition occurs (x > 1.0). Furthermore, the intensity of the absorption band at ~870–800 cm^{-1} increases and the band narrows with an increase in x. This also points to a change in the unit cell symmetry.

3.4 Dielectric spectroscopy

The results of dielectric spectroscopy investigation of $Bi_{4-x}Nd_xTi_3O_{12}$ solid solutions are presented in Figs. 4, 5, 6 and 7. The temperature dependences of dielectric permittivity ε(T) reveal anomalies of two different types (see results for the undoped sample in Fig. 4). The anomalies of the first type are frequency dependent and reflect relaxation processes. They occur at low temperature for the undoped compound, and are shifted to higher temperature as x increases. The second type of anomalies are frequency independent, and reflect the ferroelectric transition associated to the nonpolar to polar structure change. Tc amounts to 920 K for the undoped compound, and decreases to 800 K for x = 0.5, as seen in Fig. 5. As seen in the figure, a broad peak is observed near 500 K for the x = 1 compound. However, as shown in Fig. 6, this peak is frequency dependent, suggesting that ferroelectric order may be short-ranged for that composition; c.f.

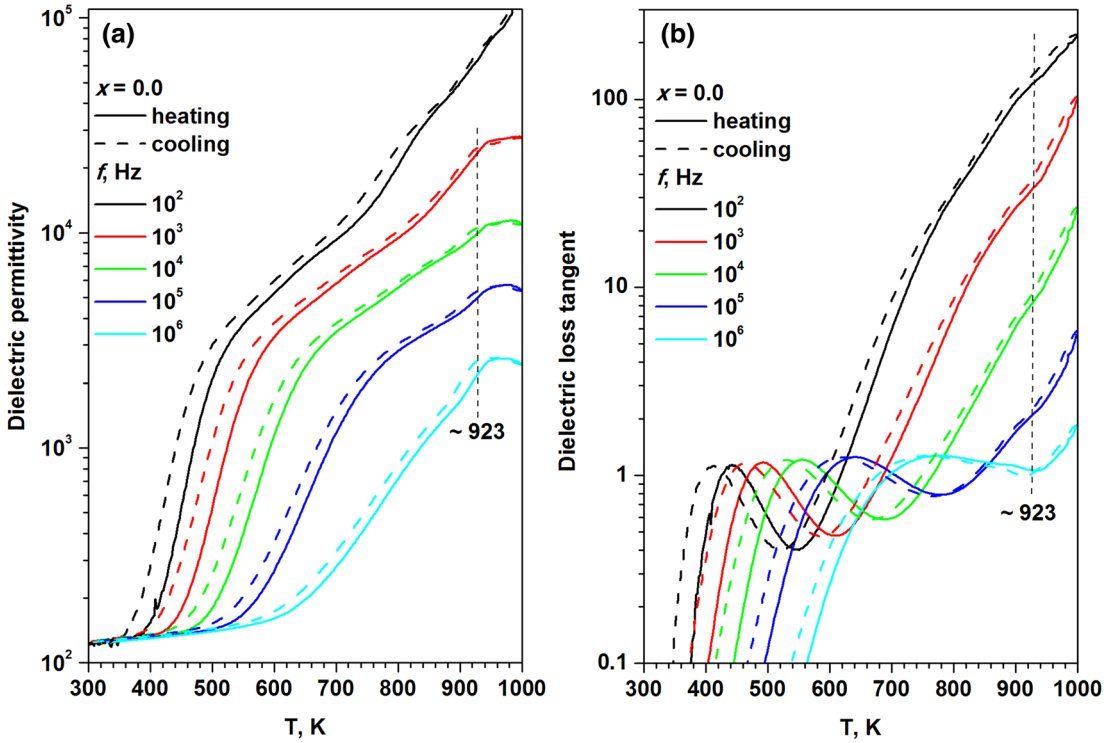

Fig. 4 Temperature dependence of **a** the dielectric permittivity ε and **b** the dielectric loss tangent of $Bi_4Ti_3O_{12}$ for different frequencies

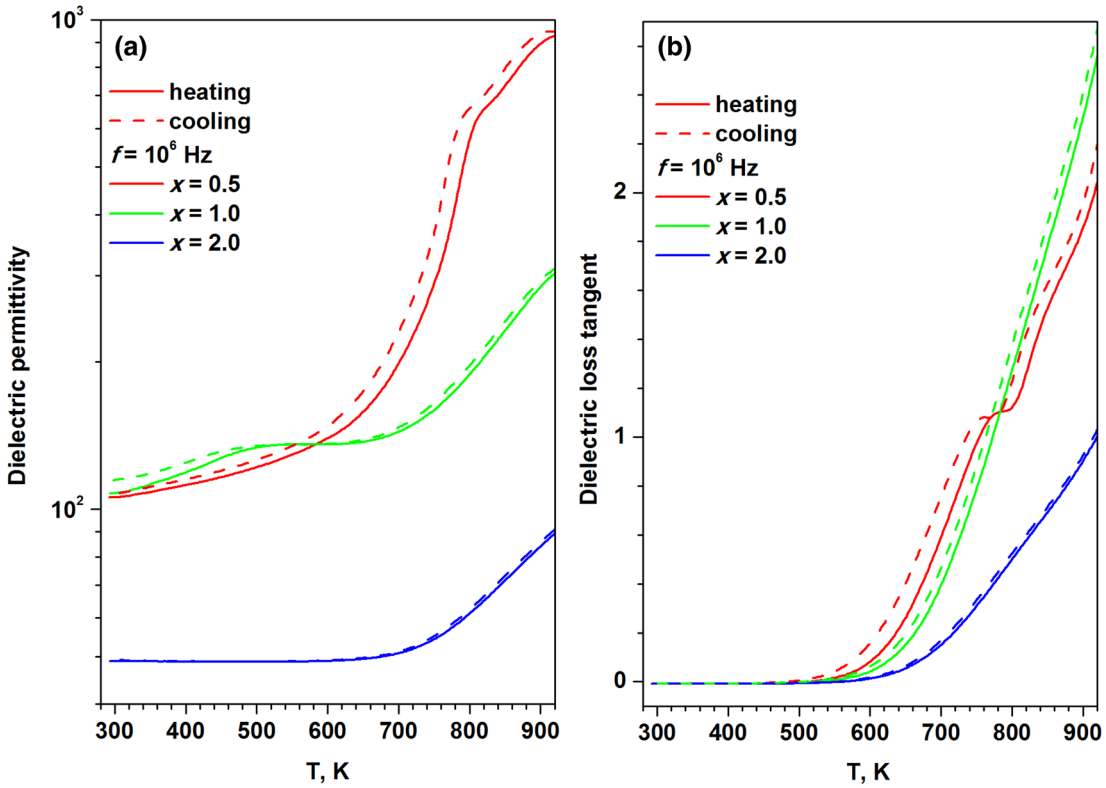

Fig. 5 Temperature dependence of **a** the dielectric permittivity ε and **b** the dielectric loss tangent of $Bi_{4-x}Nd_xTi_3O_{12}$ ceramics at $f = 10^6$ Hz

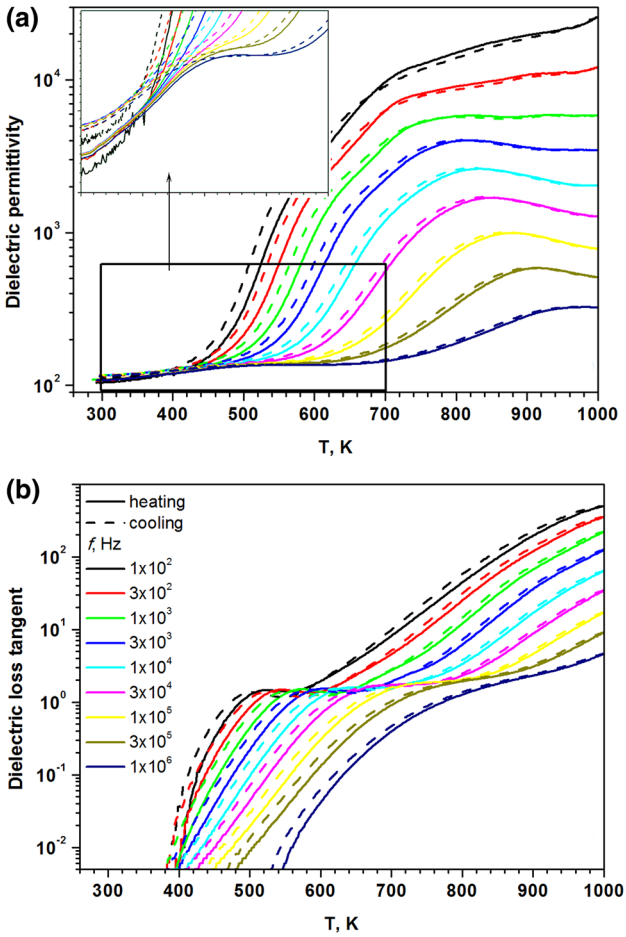

Fig. 6 The frequency dependence of **a** the dielectric permittivity ε(T) and **b** the dielectric loss tangent of $Bi_3NdTi_3O_{12}$ ceramic (x = 1). The *inset* in the *upper panel* shows a scaled view around the T = 500 K region

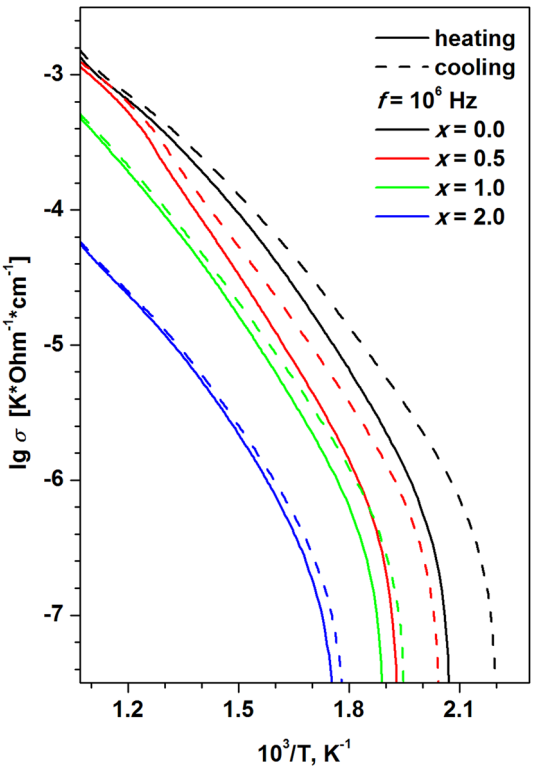

Fig. 7 Arrhenius' plots of conductivity, σ, of the $Bi_{4-x}Nd_xTi_3O_{12}$ ceramics at $f = 10^6$ Hz

SHG results. The dielectric response of the x = 1 compound is dominated by the large relaxation occurring at higher temperatures. No anomaly is observed in the ε(T) dependences of the sample with x = 2.0, confirming the earlier supposition that compounds with $x \geq 1$ have non-polar structure.

A strong increase in the conductivity of the $Bi_{4-x}Nd_xTi_3O_{12}$ ceramics occurred at temperatures greater than 530 K (Fig. 7). Such behaviour and the observed frequency dispersion indicate an oxygen ionic type conductivity in these samples. The reduction of conductivity by approximately 1.5 orders of magnitude in the investigated range of x is related to the decrease of oxygen vacancies in the crystal structure due to the stabilization of the $(Bi_2O_2)^{2+}$ layers with an increase in the Nd^{3+} content. Thus, the Nd cations reduce the bismuth losses during the high-temperature synthesis.

3.5 Magnetic measurements

The M versus T curves of the $Bi_{4-x}Nd_xTi_3O_{12}$ series recorded in the zero field cooled (ZFC) mode under a low field ($\mu_0H = 0.005$ T) and a high field ($\mu_0H = 0.5$ T) are shown in Fig. 8a, b respectively. The samples do not show any magnetic transition in the measured temperature range of 5–320 K. In order to investigate the paramagnetic behaviour of $Bi_{4-x}Nd_xTi_3O_{12}$, we have performed Curie–Weiss fits to the susceptibility data using the modified Curie–Weiss law: $\chi = \chi_0 + \frac{C}{T-\theta_{CW}}$. As representative examples, we show the fits for the two end members (x = 0 and 2.0) in Fig. 9a, b; the straight lines are the fits to the experimental data. The values of the effective magnetic moment (μ_{eff}) and the Curie–Weiss constants (θ_{CW}) obtained from the fits for the entire $Bi_{4-x}Nd_xTi_3O_{12}$ series are summarized in Table 1. There is a good agreement between the calculated spin moment per formula unit and the effective magnetic moment extracted from our fits to the experimental data. Furthermore, apart from the undoped sample (x = 0), all the other samples have a negative Curie–Weiss constant ranging between −20 and −50 K. Thus, the incorporation of Nd^{3+}

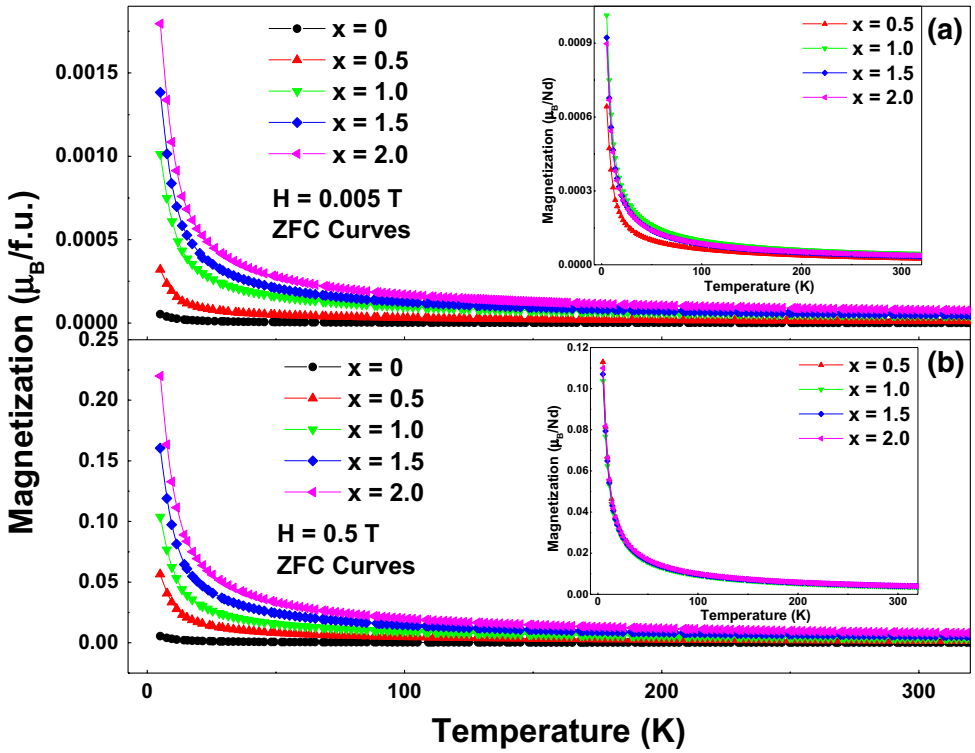

Fig. 8 M versus T curves of $Bi_{4-x}Nd_xTi_3O_{12}$ recorded under a magnetic field of **a** $\mu_0H = 0.005$ T and **b** $\mu_0H = 0.5$ T. The *insets* show the same curves for the doped samples with the magnetization plotted in units of μ_B/Nd

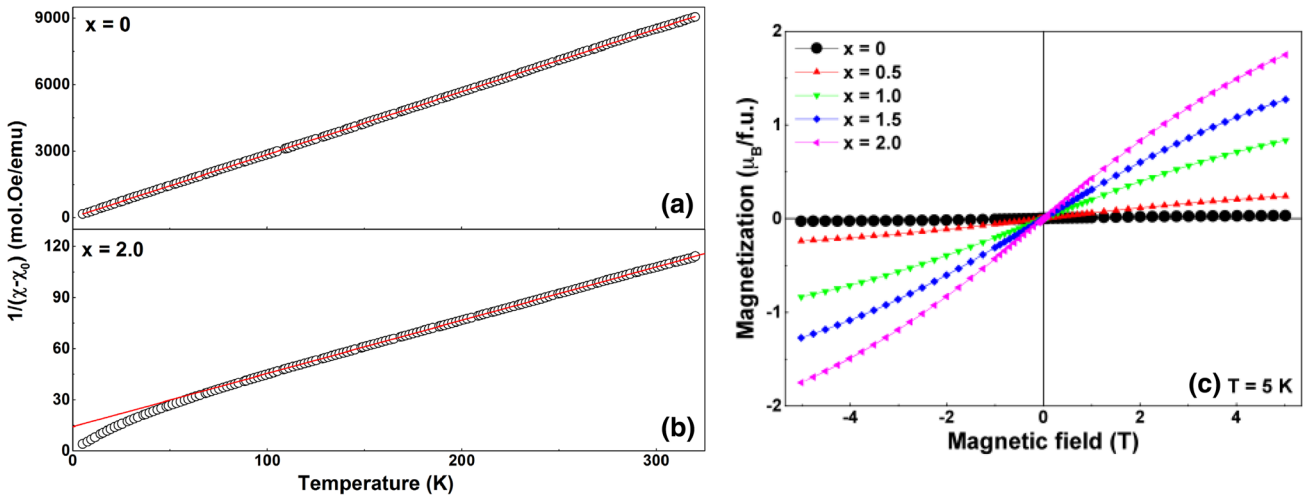

Fig. 9 Inverse magnetic susceptibility versus temperature for **a** $Bi_4Ti_3O_{12}$ and **b** $Bi_2Nd_2Ti_3O_{12}$. The *straight lines* are the fits to the experimental data (see text for details), **c** M versus H curves of $Bi_{4-x}Nd_xTi_3O_{12}$ recorded at T = 5 K

at the A-site induces significant antiferromagnetic interaction. The low temperature (T = 5 K) isothermal magnetization curves of $Bi_{4-x}Nd_xTi_3O_{12}$ are shown in Fig. 9c. The samples with $x > 0$ show a nonlinear S-shaped behaviour. However, the lack of any observable hysteresis loop indicates that the samples do not have any spontaneous magnetization.

3.6 Structural investigation

For a more quantitative assessment of the effect of Nd substitution on the phase stability, XRPD patterns of BNTO ceramics were registered (Fig. 10). All sets of reflections could be indexed in the orthorhombic structure of the parent compound (JCPDS card No.35-0795). No secondary phases were found within the detection limit of our XRPD

Table 1 Effective magnetic moments (μ_{eff}) and Curie–Weiss constants (θ_{CW}) of $Bi_{4-x}Nd_xTi_3O_{12}$ obtained from Curie–Weiss fits to the high temperature susceptibility data

Composition	μ_{eff}/f.u. (μ_B)	θ_{CW} (K)	μ_{calc} (μ_B)
$Bi_4Ti_3O_{12}$	0.53	−1 (6)	0
$Bi_{3.5}Nd_{0.5}Ti_3O_{12}$	2.34	−27 (6)	2.56
$Bi_3NdTi_3O_{12}$	3.38	−38 (6)	3.62
$Bi_{2.5}Nd_{1.5}Ti_3O_{12}$	4.03	−31 (6)	4.43
$Bi_2Nd_2Ti_3O_{12}$	5.06	−46 (6)	5.12

set up. As can be observed from Fig. 10, there seems to be very little difference in the patterns of BTO and BNTO. There is a systematic shift of the reflections to higher 2θ values with an increase in x. This is expected because of the difference in the ionic radii of Nd^{3+} (1.09 Å) and Bi^{3+} (1.17 Å); both with c. n. 8. This observation indicates that the Nd^{3+} ions in BNTO do not form minority phases or segregate from the interior grains; rather they dissolve into the perovskite lattice even for high concentrations of Nd.

The tendency of the changes in the lattice parameters with substitution of Nd^{3+} for Bi^{3+} was studied in details. For pseudo-orthorhombic $Bi_4Ti_3O_{12}$ (x = 0), the (2 0 0)/(0 2 0) reflections are well separated into two peaks in the XRD patterns (see Fig. 11). Other reflections with crystallographic index of (*hkl*)/(*khl*) were also observed to split into two peaks (data not shown here). However, these diffraction doublets gradually merged into a single peak as the Nd^{3+} concentration increased from 0.5 to 1.5, indicating an increase in the symmetry of the crystal structure. Inspection of the raw data for the samples with x = 1.5 and 2.0 and the merging of the diffraction doublet suggests that the higher doped samples crystallize in the *I*4/*mmm* tetragonal structure. The volume of the tetragonal unit cell is approximately half that of the orthorhombic unit cell. Refinements using the tetragonal space group yielded a perfect fit for the higher doped samples. Similar structural phase transformations by increasing the dopant concentration has been reported for other Ln-dopants as well (e.g., for La near x = 0.86 [44], for Eu near x = 1.2 [38], and for Sm/Fe near x = 0.4 [45]). The lattice parameters of the BNTO samples are presented in Fig. 12 and listed in Table 2. For a better comparison of the orthorhombic and tetragonal structural data, the estimated values of a_{tetra} for x = 1.5 and 2.0 were converted into the equivalent a_{ortho} applying the relation $a_{ortho} = \sqrt{2}\ a_{tetra}$. The lattice parameters and unit cell volume of the BNTO samples decrease monotonously with increasing concentration of Nd.

The difference between the *a* and *b* lattice parameters was found to be extremely small for the sample with concentration x = 1.0, For the solid solution with x = 1.0, the Rietveld refinement of the diffractions pattern gave very similar results for the polar *B*2*cb* and nonpolar *I*4/*mmm* structural models, thus making the determination of the true symmetry of the compounds on the basis of XRPD data only difficult. However, SHG data clearly showed that the structure of this composition is noncentrosymmetric at room temperature (see Fig. 2).

For describing the structure of BNTO ($x \leq 1.0$) at room temperature, there are two existing models (orthorhombic *B*2*cb* [46–49] and monoclinic *B*1*a*1 [50, 51]) that are difficult to distinguish. Structural refinements of the materials with x = 0, 0.5, and 1.0 were performed using the space group *B*2*cb* (No. 41) with the reported crystallographic data of $Bi_4Ti_3O_{12}$ [47] as a starting model. No crystallographic ordering between the Bi^{3+} and the Nd^{3+} cations was observed. Site occupancies for the Bi/Nd distribution over the two possible sites were refined using the split-atom model with the total occupancy of Bi^{3+}:Nd^{3+} fixed to {(4 − x)/4}:x/4 as expected from the synthesis and results of EDS analysis. Careful inspection of the XRPD patterns for samples with x = 0, 0.5, and 1.0 revealed no deviation from the orthorhombic symmetry within the resolution of the instrument. On the other hand, we could not obtain a stable refinement of the *B*1*a*1 model using our data due to very high pseudosymmetric correlations and no deviation from metric orthorhombic symmetry in the frame of standard deviation.

The orthorhombic structural model has two sites containing Bi^{3+} with different coordination environments (Fig. 13). The $[Bi_2O_2]$ layer site (Bi2) is an 8-coordinate position, while the perovskite A-site (Bi1) adopts 12-coordination. There are two Ti^{4+} containing sites, the perovskite B-sites, both of which are distorted octahedral sites with the octahedra rotated around the principal unit cell axes. It is these octahedral distortions, together with the co-operative displacement of the Bi1 site that are considered keys to the ferroelectric properties of this family of materials.

The Nd substitution occurs primarily on the perovskite A-site (Bi1) and not on the $[Bi_2O_2]$ layer site (Bi2). However, our XRPD studies reveal that Nd^{3+} occupies both sites for x = 1.5 and 2.0, although substitution on the A-site was more favorable.

The tetragonal structure of BNTO at room temperature for samples with x = 1.5 and 2.0 is identical to the structure of the high temperature phase of BTO that is stable only above its T_C (~920–930 K). The structural model of the tetragonal phase proposed in [32, 52] was modified and Bi^{3+} and Nd^{3+} cations were allowed to randomly occupy the two available cation sites. Bi:Nd stoichiometry was constrained to remain constant; the z co-ordinates and isotropic thermal parameters of Bi^{3+} and Nd^{3+} occupying the two distinct cation sites were constrained to be equal. In the final step, the O1 oxygen atom was allowed to displace from the ideal 4e position, (0, 1/2, 0), to a new 8j position,

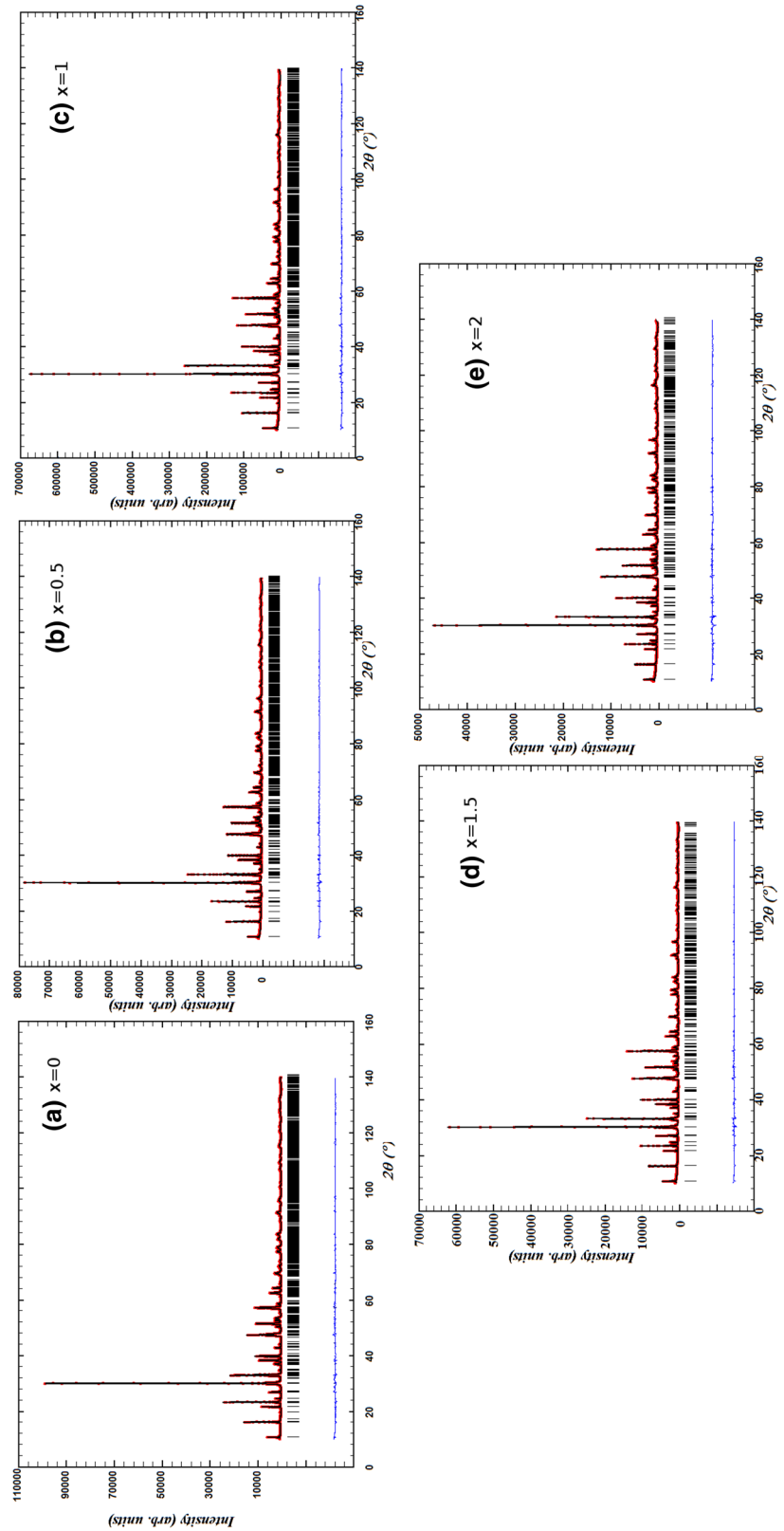

Fig. 10 The observed, calculated, and difference plots for the fit to the XRPD patterns of $Bi_{4-x}Nd_xTi_3O_{12}$ after Rietveld refinement of the atomic structure at 295 K

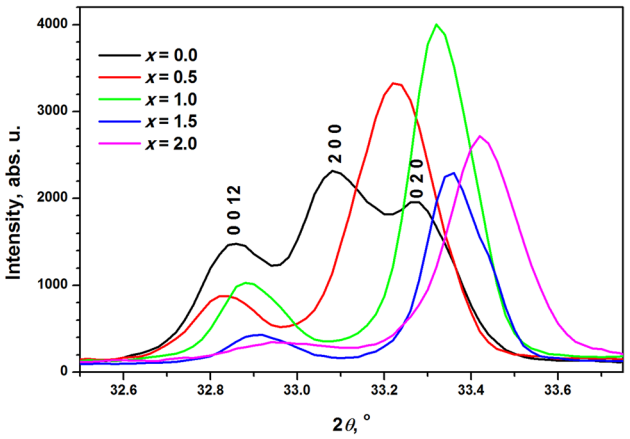

Fig. 11 Overlapping behavior of the (200) and (020) Bragg reflections in $Bi_{4-x}Nd_xTi_3O_{12}$

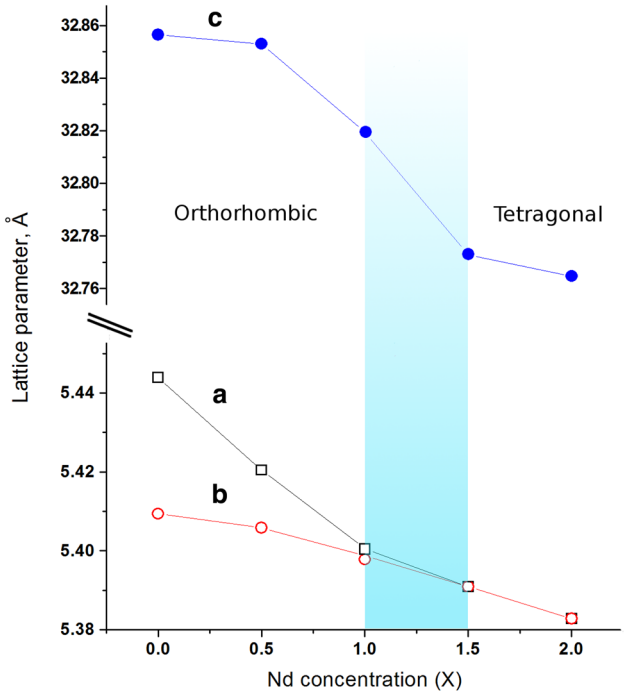

Fig. 12 Concentration dependence of the lattice parameters *a*, *b*, and *c* of $Bi_{4-x}Nd_xTi_3O_{12}$ at room temperature

(x, 1/2, 0), corresponding to a rotation of the Ti_1 octahedra about the ⟨0 0 1⟩ axis.

The structural parameters for all investigated compounds are tabulated in Table 2 (final Rietveld plots are presented in Fig. 10), and the corresponding bond distances are shown in Table 3. Figure 13 illustrates the crystal structure of BTO (x = 0) and BNTO (x = 2) on the basis of the refined structural parameters. No evidence for ordering was observed, however, the Bi^{3+} in the A site of the perovskite block tends to be preferentially substituted by Nd^{3+} compared to the $(Bi_2O_2)^{2+}$ rock-salt unit. A similar site preference for La^{3+} has been reported before [53–55].

Deviations from the tetragonal symmetry are caused by displacements of the Bi^{3+}/Nd^{3+} with corresponding cooperative tilting and distortion of the TiO_6 octahedra in order to satisfy the bonding requirements at the four available cation sites. The Bi_2O_2 layers and TiO_6 octahedra in the perovskite units are distorted and the TiO_6 octahedron along the *c*-axis are buckled. These displacements are the primary cause of the remnant polarization of BNTO at room temperature.

The remarkable decrease of the orthorhombic distortion with increase in Nd concentration is correlated with the cationic polar displacements and degree of tilting of the octahedra. The observed trends of the bond distances allowed us to conclude that the Bi(1) cation located inside the perovskite block has a coordination number 12. With an increase in the Nd concentration, the range of Bi1–O bond lengths gradually decreases and these bonds become more equivalent. A similar situation is observed for Bi_2 in the $[Bi_2O_2]$ block in spite of its different coordination number (9). The coordination around the Ti1 and Ti2 sites are relatively insensitive to Nd doping. Calculation of bond valence sums (BVS) for the Bi and Ti sublattices yielded values (see Table 4) that are quite close to the optimal values. Polyhedral analysis shows drastic off-center displacements for the two Bi atoms, together with distortions of both the Ti octahedral sites. The strong preference for the Bi cations to occupy a highly distorted coordination polyhedral is related to their stereochemically active lone electron pair. In the case of compounds with $x > 0$ where the A-sites are partly occupied by Nd^{3+} instead of Bi^{3+}, the observed orthorhombic distortion is significantly less and these polyhedra are more regular.

4 Discussion

As shown in Table 2, the unit cell volume and orthorhombicity exhibit the expected decrease with increase in Nd^{3+} concentration (also see Fig. 12). The gradual decrease of the orthorhombic distortion and the eventual transition to a tetragonal symmetry for $x \geq 1.5$ can be correlated with key structural features, such as cationic displacements from ideal positions and the degree of tilting of the octahedra. Inspection of the bond lengths in Tables 3 and 4 reveals several trends. The Bi cation prefers an asymmetrical arrangement of the anion neighbors because of its nonspherical electron configuration. The number of "ferroelectric-active" cations decreases when a symmetrical Nd^{3+} replaces Bi^{3+}. The smaller effective size of Nd^{3+} could

Table 2 Results of the Rietveld refinements of the crystal structure of $Bi_{4-x}Nd_xTi_3O_{12}$ samples at room temperature using XRPD data

Phase	x = 0	x = 0.5	x = 1.0	x = 1.5	x = 2.0
a,Å	5.4439(2)	5.4204(2)	5.4005(2)	3.8119(2)	3.8097(2)
b,Å	5.4094(2)	5.4059(2)	5.3987(2)	3.8119(2)	3.8097(2)
c,Å	32.8565(8)	32.8523(8)	32.8194(7)	32.7730(4)	32.7670(4)
V,Å^3	967.6	962.6	956.9	476.2	475.6
g, 10^{-3}	6.36	2.68	0.334		
s.g	*B 2 c b*	*B 2 c b*	*B 2 c b*	*I/4 mm*	*I/4 mm*
EDS Bi, Nd, Ti at.%	*56.9, 0, 43.1*	*49.7, 6.9, 43.4*	*42.6, 14.1, 43.3*	*35.6, 21.3, 43.1*	*28.5, 28.3, 43.2*
Bi1/Nd1					
n Bi/Nd	0.99(2)/–	0.74/0.26(2)	0.51/0.49(2)	0.95/0.05(2)	0.81/0.19(2)
x/a	0	0	0	0	0
y/b	0.9979(6)	0.9963(4)	0.9954(4)	0	0
z/c	0.0666 (1)	0.0669(1)	0.0670 (1)	0.2890(1)	0.2889(1)
Beq(Å^2)	1.18(3)	1.23(4)	1.27(6)	0.98(5)	0.92(4)
Bi2/Nd2					
n Bi/Nd	1.00(2)/–	0.99(2)/–	0.99/0.01(2)	0.29/0.71(2)	0.19/0.81(2)
x/a	0.0021(7)	0.0024(8)	0.0028(9)	0	0
y/b	0.0151(8)	0.0158(6)	0.0162(7)	0	0
z/c	0.2111(1)	0.2113(2)	0.2115(2)	0.4332(1)	0.4336(7)
Beq(Å^2)	0.97(3)	1.06(5)	0.79(2)	0.89(4)	0.84(4)
Ti1					
n	1.01(2)	0.98(2)	0.99(2)	1.00(2)	1.01(2)
x/a	0.0491(8)	0.0449(7)	0.0411(9)	0	0
y/b	0	0	0	0	0
z/c	1/2	1/2	1/2	0	0
Beq(Å^2)	0.56(3)	0.62(4)	0.67(2)	0.72(4)	0.63(4)
Ti2					
n	0.99(1)	1.01(2)	1.02(2)	1.00(2)	0.99(2)
x/a	0.0327(8)	0.0303(7)	0.0298(9)	0	0
y/b	0.0026(9)	0.0028(9)	0.0031(8)	0	0
z/c	0.3713(2)	0.3709(2)	0.3706(2)	0.1286(3)	0.1282(3)
Beq(Å^2)	0.45(2)	0.53(4)	0.51(2)	0.67(4)	0.52(4)
O1					
n	0.98(2)	0.99(2)	0.98(2)	0.98(2)	0.99(2)
x/a	0.3231(9)	0.3278(8)	0.3302(8)	0.0880(5)	0.083(6)
y/b	0.2634(8)	0.2645(9)	0.2652(8)	0.5	0.5
z/c	0.0073(2)	0.0079(4)	0.0085(3)	0	0
Beq(Å^2)	0.97(5)	0.94(5)	1.13(6)	1.32(5)	1.43(4)
O2					
n	1.02(2)	0.98(2)	0.99(2)	0.98(2)	1.01(2)
x/a	0.2685(8)	0.2704(9)	0.2721(9)	0	0
y/b	0.2590(9)	0.2615(8)	0.2656(8)	0	0
z/c	0.2501(2)	0.2518(3)	0.2536(2)	0.0606(3)	0.0596(5)
Beq(Å^2)	1.17(5)	1.11(4)	1.22(5)	1.21(5)	1.13(6)
O3					
n	0.98(2)	0.98(2)	0.98(2)	0.99(2)	0.98(2)
x/a	0.0849(9)	0.0834(7)	0.0826(8)	0	0
y/b	0.0595(8)	0.0583(7)	0.0562(8)	0.5	0.5
z/c	0.4398(3)	0.4391(2)	0.4380(3)	0.1164(5)	0.1149(4)
Beq(Å^2)	1.21(6)	1.12(3)	1.15(2)	1.24(4)	1.32(3)

Table 2 (continued)

Phase	x = 0	x = 0.5	x = 1.0	x = 1.5	x = 2.0
O4					
n	0.97(2)	0.98(2)	0.97(2)	0.98(2)	0.99(2)
x/a	0.0532(11)	0.0521(9)	0.0512(11)	0	0
y/b	0.9472(12)	0.9511(8)	0.9523(9)	0	0
z/c	0.3187(2)	0.3189(2)	0.3191(2)	0.1824(6)	0.1841(6)
Beq(Å^2)	1.46(6)	1.51(5)	1.39(6)	1.32(6)	1.27(5)
O5					
n	0.98(2)	0.97(2)	0.97(2)	0.99(2)	0.98(2)
x/a	0.2876(9)	0.2907(9)	0.2921(11)	0	0
y/b	0.2396(8)	0.2361(7)	0.2332(7)	0.5	0.5
z/c	0.1114(3)	0.1112(2)	0.1109(3)	0.25	0.25
Beq(Å^2)	1.08(5)	0.97(4)	1.11(2)	0.72(4)	0.65(4)
O6					
n	1.02(2)	1.01(2)	1.02(2)		
x/a	0.2214(11)	0.2205(11)	0.2193(12)		
y/b	0.2093(8)	0.2087(7)	0.2076(8)		
z/c	0.8760(2)	0.8764(2)	0.8771(2)		
Beq(Å^2)	0.98(5)	0.86(5)	1.03(5)		
Ti1–O1–Ti1,deg	163.4(6)	161.2(5)	157.9(6)		
Ti1–O3–Ti2,deg	158.8(8)	159.1(7)	159.6(4)		
Ti2–O5–Ti2,deg	147.1(7)	145.9(8)	144.1(5)		
Ti2–O6–Ti2,deg	155.1(5)	154.7(6)	152.3(5)		
Rp	5.16	5.08	5.04	5.18	5.11
Rwp	6.71	6.63	6.59	6.01	6.66
R_B	4.54	4.39	5.04	4.92	4.41
χ2	1.23	1.28	1.31	1.16	1.19

Standard deviations of occupation factors are generally less than 0.02. Orthorhombicity parameter (g) was calculated using the equation $g = 2(a-b)/(a+b)$

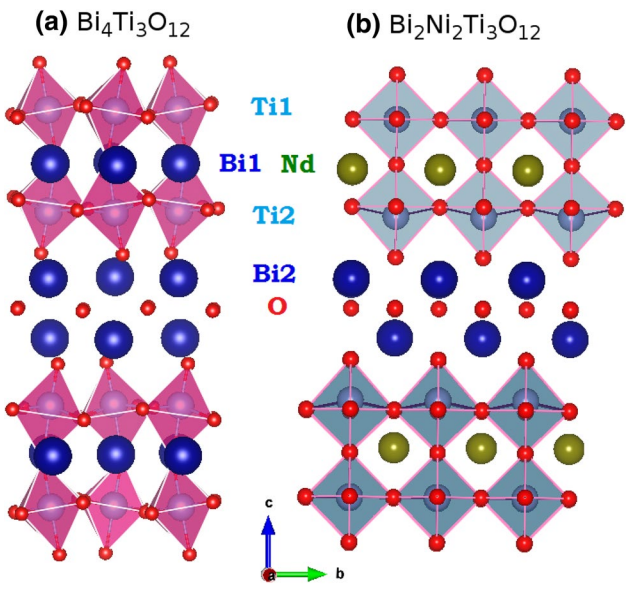

Fig. 13 Schematic representation of the $Bi_{4-x}Tb_xTi_4O_{12}$ structures: **a** x = 0 and **b** x = 2; drawn using VESTA [54]

make the geometrical mismatch even more pronounced resulting in a decrease of T_C.

The coordination number of Bi1 in the perovskite site may be regarded as 12. In the tetragonal structure (x > 1), these consist of three symmetry-equivalent sets of four bond distances. In the orthorhombic structure of BNTO (x < 1), these distances become inequivalent, and the range of bond distances decreases with decrease in the concentration (see Table 3). A similar effect was observed for Bi2 in the $[Bi_2O_2]$ fluorite-type layer for which the ideal coordination number is eight (square antiprism of four O2 atoms within the $[Bi_2O_2]$ layer and four O4 atoms form the apexes of the perovskite blocks). With decrease in the Nd concentration, the range of these bond lengths (distortion) increases. The octahedral coordination of Ti1 and Ti2 sites is relatively unaffected by change in concentration, becoming slightly less regular for samples with lower values of x. The octahedral tilts increase with decrease in x. The bond valence sum (BVS) analysis [56] indicated some

Table 3 Selected bond distances (Å) from XRPD data refinements of $Bi_{4-x}Nd_xTi_3O_{12}$ samples at room temperature

Cation	x = 0	x = 0.5	x = 1.0		x = 1.5	x = 2.0
Bi1/Nd1						
O1	2.993	3.003	3.029	O4 x4	2.854	2.835
O1	3.316	3.345	3.389			
O1	2.529	2.511	2.472			
O1	2.905	2.913	2.902			
O3	2.452	2.420	2.418			
O3	3.080	3.078	3.065			
O3	2.291	2.286	2.277	O5 x4	2.296	2.293
O3	3.206	3.182	3.163			
O5	2.515	2.506	2.482			
O5	2.349	2.344	2.352			
O6	2.502	2.474	2.443			
O6	2.879	2.859	2.842			
Bi2/Nd2						
O2	2.341	2.376	2.424	O1 x2	2.696	2.693
O2	2.376	2.339	2.301			
O2	2.332	2.302	2.284	O1 x2	3.132	3.109
O2	2.179	2.191	2.212			
O4	3.237	3.222	3.211	O2 x4	2.706	2.703
O4	2.549	2.564	2.567			
O4	2.641	2.640	2.637	O3 x4	2.506	2.481
O4	3.163	3.145	3.127			
O6	3.331	3.341	3.343			
Ti1						
O1 x2	1.980	2.009	2.070	O1 x4	1.935	1.931
O1 x2	1.898	1.870	1.820	O2 x2	1.985	1.953
O3 x2	2.013	2.036	2.069			
Ti2						
O3	2.289	2.279	2.259	O2	2.242	2.248
O4	1.752	1.734	1.718			
O5	2.067	2.102	2.124	O3 x4	1.948	1.954
O5	1.955	1.924	1.915			
O6	1.873	1.878	1.868	O4	1.762	1.832
O6	2.036	2.033	2.038			

Standard deviation is limited to 0.009 and 0.02 for cations and anions, respectively

underbonding at both Bi sites, in particular at the Bi1 perovskite site. The Ti sites are slightly overbonded.

The lone electron pairs of the Bi^{3+} cations play a crucial role in the structural distortion in the ferroelectric phase owing to the correlated reorientation [15, 57] in order to optimize its bonding to the neighboring anions. The structural mechanism of the concentration-induced phase transformation from *I*4/*mmm* to *B*2*cb* in BNTO is not trivial because a direct transition is not possible. Modes of more than one irreducible representation must be invoked in order to explain the symmetry breaking. The change of symmetry is associated with a combination of rotations of the B-octahedra and cation displacements compared to the prototype phase. A direct comparison of the *I*4/*mmm* and *B*2*cb* structures using group-subgroup analysis performed using the AMPLIMODES software [58–60] revealed that the expected symmetry changes could follow the path *I*4/*mmm*→*F*2*mm*→*B*2*cb* with one intermediate phase. All modes related to this structural transformation were calculated although the presence of two of them ($X3^+$ and *Eu*) is sufficient to prove the presence of polar orthorhombic distortion. The $X3^+$ mode is related to an octahedral tilting around the *x* axis within the perovskite slabs, together with correlated displacements of the Bi atoms. This mode is responsible for the duplication of the unit cell. *Eu* is a polar mode related to a relative displacement of the Bi sublattice

Table 4 Polyhedral analysis of $Bi_{4-x}Nd_xTi_3O_{12}$ samples at 295 K (x-concentration of Nd, δ—cation shift from centroid, ξ—average bond distance, V—polyhedral volume, Δ—polyhedral volume distortion)

Cation	x	δ(Å)	ξ (Å)	V(Å^3)	Δ	Valence
Compositions with s.g *B2cb*						
Bi1/Nd1 (c.n.=12)	0	0.069	2.749 ± 0.354	48.2(1)	0.028	2.90
	0.5	0.038	2.743 ± 0.361	47.8(1)	0.070	2.98
	1.0	0.056	2.734 ± 0.365	47.3(1)	0.071	3.07
Bi2/Nd2 (c.n.=9)	0	0.439	2.683 ± 0.442	36.9(1)	0.101	2.94
	0.5	0.435	2.681 ± 0.441	36.8(1)	0.098	2.93
	1.0	0.413	2.679 ± 0.444	37.2(1)	0.097	2.97
Ti1 (c.n.=6)	0	0.092	1.964 ± 0.053	9.9(1)	0.006	4.05
	0.5	0.087	1.972 ± 0.080	10.0(1)	0.006	4.01
	1.0	0.085	1.983 ± 0.104	10.2(1)	0.007	3.94
Ti2 (c.n.=6)	0	0.066	1.996 ± 0.182	10.1(1)	0.021	4.04
	0.5	0.082	1.990 ± 0.189	9.9(1)	0.023	4.15
	1.0	0.106	1.982 ± 0.187	9.7(1)	0.026	4.21
Compositions with s.g. *I4/mmm*						
Bi1/Nd1 (c.n.=9)	1.5	0.819	2.574 ± 0.299	26.8(1)	0.258	2.81
	2.0	0.838	2.564 ± 0.289	26.1(1)	0.270	2.84
Bi2/Nd2 (c.n.=12)	1.5	0.041	2.707 ± 0.219	46.8(1)	0.064	2.68
	2.0	0.037	2.695 ± 0.221	46.1(1)	0.062	2.73
Ti1 (c.n.=6)	1.5	0	1.952 ± 0.026	9.9(1)	0	4.15
	2.0	0	1.938 ± 0.011	9.7(1)	0	4.31
Ti2 (c.n.=6)	1.5	0.116	1.964 ± 0.149	9.6(1)	0.009	4.23
	2.0	0.161	1.983 ± 0.139	9.9(1)	0.016	4.01

along the *x* axis with respect to the slabs of the TiO_6 octahedra. This mode causes the spontaneous polarization along the *x* axis, and is thus, primarily responsible for the ferroelectric properties of the room temperature phase. The atomic displacements that are responsible for the phase transformation primarily consist of polar cation shifts along the [100] direction and tilting of the TiO_6 octahedra around the [100] and [001] directions. The hypothetical phase *F*2*mm* has not been detected, although the presence of possible intermediate phases has been suggested recently [61].

The correlated motions of the atoms within the perovskite and fluorite blocks are out-of-phase with each other as shown in Fig. 13 and the transition is associated with the opposite movement of the fluorite- and perovskite-like layers.

The coordination environment of the Ti2 cation in the perovskite-type layer is considerably distorted from ideal octahedral geometry. This distortion results in a significant buckling of the outer TiO_2 planes. The coordination environment of the Ti1 cation also appears to be distorted, although the nature of this distortion, involving two longer apical Ti–O2 bonds and four shorter equatorial Ti–O1 bonds is symmetric, in contrast to the asymmetric distortion of the Ti2 octahedron. The shape of the Ti octahedra of the paraelectric phase remains nearly unchanged in the ferroelectric phase. The TiO_6 octahedra rotate in the *a*-*b* plane as well as tilt away from the *c* axis.

Using the tolerance factor arguments in Ref [32]. it was found that there is considerable strain at the interface between the fluorite- and perovskite-type layers in the structure of BNTO. This strain, present in $Bi_4Ti_3O_{12}$ and $Bi_2Nd_2Ti_3O_{12}$, is relieved in different ways, namely, by octahedral tilting and lowering of symmetry, and by cation disorder, respectively.

The structural studies of the BNTO system have demonstrated the presence of significant cation disorder. Thus, the structural formula of $Bi_2Nd_2Ti_3O_{12}$ is perhaps more properly formulated as $(Bi_{0.81}Nd_{0.19})_2(Nd_{0.81}Bi_{0.19})_2Ti_3O_{12}$, so as to reflect the cross substitution of 19% of the Nd/Bi cations onto the Bi/Nd sites in the fluorite- and perovskite-type layers, respectively.

It is not possible to discard the possibility of the presence of some kind of ordered magnetism for other rare-earth doped compounds in the $Bi_{4-x}Ln_xTi_3O_{12}$ series. Magnetic properties of these systems, depending on the ionic radius and electronic structure of the substituents, should be investigated in details. At the same time, recent results suggest that more promising results can be obtained in cases where Ln substitution in the ferroelectric Aurivillius phases is accompanied by B-site doping of the perovskite-type units

with magnetically- active transition-metal ions [62, 63]. In such cases, the magnetic moments of the A-site and B-site transition metal subsystem will provide more remarkable contribution to the resultant magnetic properties [64, 65].

There has been a number of studies of the doping of rare earth and transition metal elements at the A and B-sites in $Bi_4Ti_3O_{12}$ [29, 35, 37, 45, 62, 67–70]. Although a majority of these studies focuses on the effects that such doping has on the microstructural and ferroelectric properties of $Bi_4Ti_3O_{12}$ [35, 66–70], it is important to investigate the magnetic properties also, especially when the ultimate goal is multiferroism. However, till date there has been no report of long range magnetic order in rare earth doped $Bi_4Ti_3O_{12}$ [29, 35]. Rather, composite phases, such as nLaFeO$_3$-$Bi_4Ti_3O_{12}$ thin films [44], $BiFeO_3/Bi_4Ti_3O_{12}$ bilayer films [64], and multilayer structures of $Bi_{3.5}Nd_{0.5}Ti_3O_{12}/CoFe_2O_4$ [65] have been reported to exhibit long range magnetic order and magnetoelectric coupling at room temperature. Doping transition metal elements at the B-site in the presence [45, 66] or absence [62] of rare earth doping at the A-site has also yielded magnetoelectric properties. Our results on BNTO show that the compounds are paramagnets, but with underlying antiferromagnetic interactions. Moreover, the strength of the underlying interactions increases with increase in Nd concentration as evidenced by an increase in the value of the Curie–Weiss constant. It is quite possible that a further increase in the Nd concentration will induce long range order in the system. Efforts are ongoing to prepare phase pure samples with a higher concentration of Nd. However, it should be noted that realizing completely phase pure samples with such a high concentration of Nd is nontrivial and requires application of high pressure during synthesis.

5 Conclusions

The structural, ferroelectric, and magnetic properties of $Bi_{4-x}Nd_xTi_3O_{12}$ solid solutions ($x = 0.0$, 0.5, 1.0, 1.5, and 2.0) prepared by traditional solid-state reaction technique were investigated. The concentration evolution of the XRPD patterns reveals a weakening of the ferroelectric orthorhombic lattice distortion (s.g. *B2cb*) with increase in the Nd concentration for $x < 1$ and, finally, a transition to the paraelectric tetragonal structure (s.g. *I4/mmm*) for higher Nd content. XRPD results confirm this phase transition via the observation of the diffraction peaks corresponding to the (200) and (020) planes of BTO coalescing into a single peak for BNTO with $x = 1.5$. Accordingly, the ferroelectric order is weakened by the Nd doping, and the Curie temperature rapidly decreases with increasing x up to $x = 1$. All samples are found to be paramagnetic, albeit with significant magnetic interaction.

Acknowledgements Financial support from the Swedish Research Council (VR), the Swedish Foundation for International Cooperation in Research and Higher Education (STINT) and the Russian Foundation for Basic Research is gratefully acknowledged.

References

1. M. Fiebig, T. Lottermoser, D. Meier, M. Trassin, Nat. Rev. Mater. **1**, 16046 (2016)
2. K. Wang, J.-M. Liu, Z. Ren, Adv. Phys. **58**, 321–448 (2009)
3. J.F. Scott, NPG Asia Mater. **5**, e72 (2013)
4. N. Spaldin, *Magnetic Materials: Fundamentals and Applications*, 2nd edn. (Cambridge University Press, Cambridge, 2010)
5. J.F. Scott, Nat. Mater. **6**, 256–257 (2007)
6. J.F. Scott, J. Mater. Chem. **22**, 4567–4574 (2012)
7. M.M. Vopson, Crit. Rev. Solid State Mater. Sci. **40**, 223–250 (2015)
8. D.M. Lin, D.Q. Xiao, J.G. Zhu, J. Funct. Mater. **34**, 491–495 (2003)
9. F.Q. Zhang, Y.X. Li, J. Inorg. Mater. **29**, 449–460 (2014)
10. B.H. Park, B.S. Kang, S.D. Bu, T.W. Noh, J. Lee, W. Jo, Nature **401**, 682 (1999)
11. U. Chon, H.M. Jang, M.G. Kim, C.H. Jang, Phys. Rev. Lett. **89**, 087601 (2002)
12. C.J. Lu, X.L. Liu, X.Q. Chen, C.J. Nie, G.L. Rhun, S. Senz, D. Hesse, Appl. Phys. Lett. **89**, 062905 (2005)
13. J. Li, P. Li, J. Yu, Study on Substitution Effect of $Bi_4Ti_3O_{12}$ Ferroelectric Thin Films in"Ferroelectrics", 1st edn. (InTech China, Coondoo, 2010), pp. 119–138
14. X.Y. Mao, F.W. Mao, X.B. Chen, Integr. Ferroelectr. 79, 155–161 (2006)
15. R.W. Wolfe, R.E. Newnham, J. Electrochem. Soc. **116**, 832–835 (1969)
16. R.A. Armstrong, R.E. Newnham, Mater. Res. Bull. **7**, 1025–1034 (1972)
17. E.C. Subbarao, J. Phys. Chem. Solids **23**, 665–676 (1962)
18. E.C. Subbarao, Ferroelectrics 12, 33–41 (1996)
19. T. Jardiel, A.C. Caballero, M. Villegas, J. Ceram. Soc. Jpn. 116, 511–518 (2008)
20. A.Y. Birenbaum, C. Ederer, Phys. Rev. B **90**, 214109 (2014)
21. A.Y. Birenbaum, C. Ederer, Appl. Phys. Lett. **108**, 082903 (2016)
22. U. Chon, H.M. Jang, M.G. Kim, C.H. Chang, Phys. Rev. Lett. **89**, 087601–087604 (2002)
23. D. Urushihara, M. Komabuchi, N. Ishizawa, M. Iwata, K. Fukuda, T. Asaka, J. Appl. Phys. **120**, 142117 (2016)
24. T. Watanabe, T. Kojima, T. Sakai, H. Funakubo, M. Osada, Y. Noguchi, M. Miyayama, J. Appl. Phys. **92**, 1518–1521 (2002)
25. D.Y. Guo, C.B. Wang, Q. Shen, L.M. Zhang, M.Y. Li, J. Liu, Appl. Phys. A **97**, 877–881 (2009)
26. C. Liu, D. Guo, C. Wang, J. Mater. Sci. **23**, 802–806 (2012)

27. M.K. Jeon, Y. Kim, S. Nahm, J.M. Sohn, C.H. Jung, S.I. Woo, J. Phys. D **40**, 4647–4652 (2007)
28. W. Ye, C. Lu, P. You, K. Liang, Y. Zhou. J. Appl. Cryst. **46**, 798–800 (2013)
29. R. Muralidharan, T.H. Jang, C.H. Yang, Y.H. Jeong, S.H. Kang, T.Y. I. W. Kim, T.Y. Koo. J. Phys.: Conf. Ser **200**, 012135 (2010)
30. S.N. Achary, S.J. Patwe, P.S.R. Krishna, Pramana. J. Phys **71**, 935–940 (2008)
31. J. Arreguín-Zaval, M. E. Villafuerte-Castrejón, F. González, Mater. Charact. 60, 219–224 (2009)
32. N.C. Hyatt, J.A. Hriljac, T.P. Comyn, Mater. Res. Bull **38**, 837–846 (2003)
33. Y.M. Kan, G.J. Zhang, P.L. Wang, J. Y. B. Cheng, European Ceram. Soc **28**, 1641–1647 (2008)
34. X. Mao, H. Sun, W. Wang, Appl. Phys. Lett. **102**, 072904 (2013)
35. K. Nishimura, T. Yoshioka, T. Yamamoto, IEEE Transac. Magn. 50, 2502306 (2014)
36. F.X. Wu, Z. Chen, Y.B. Chen, S.T. Zhang, J. Zhou, Y.Y. Zhu, Y.F. Chen, Appl. Phys. Lett. **98**, 212501 (2011)
37. V.A. Khomchenko, G.N. Kakazei, Y.G. Pogorelov, J.P. Araujo, M.V. Bushinsky, D.A. Kiselev, A.L. Kholkin, J.A. Paixão, Mater. Lett. **64**, 1066–1068 (2010)
38. M.E. Villafuerte-Castrejon, F. Camacho-Alanıs, F. Gonzalez, A. Ibarra-Palos, G. Gonzalez, L. Fuentes, J.L. Bucio, Eur. Ceram. Soc. **27**, 545–549 (2007)
39. J. Rodrigues-Carvajal, Physica B **192**, 55–69 (1993)
40. T.B. Zunic, I. Vickovic, IVTON-a program for the calculation of geometrical aspects of crystal structures and some crystal chemical applications. J. Appl. Crystallogr. **29**, 305–306 (1996)
41. S.K. Kurtz, T.T. Perry, J. Appl. Phys **39**, 3798–3813 (1968)
42. Y. Kan, P. Li, Y. Cheng, D. Yan, Mater. Lett. **56**, 910–914 (2002)
43. R. D. Shannon, Acta Crystallogr. A32, 751–767 (1976)
44. D. Wu, B. Yang, A. Li, Phase Trans. 82, 146–155 (2009)
45. J. Paul, S. Bhardwaj, K.K. Sharma, R.K. Kotnal, R. Kumar, J. Alloys Compds. **634**, 58–64 (2015)
46. J.F. Dorrian, R.E. Newnham, D.K. Smith, M.I. Kay, Ferroelectrics **3**, 17 (1971)
47. C.H. Hervoches, P. Lightfoot, Chem. Mater. **11**, 3359 (1999)
48. Y.I. Kim, M.K. Jeon, Mater. Lett. **58**, 1889–1893 (2004)
49. K.R. Chakraborty, S.N. Achary, S.J. Patwe, P.S.R. Krishna, A.B. Shinde, A.K. Tyagi, Ceram. Int. 33, 601–604 (2007)
50. Y. Shimakawa, Y. Kubo, Y. Tauchi, S. Asano, T. Kamiyama, F. Izumi, Z. Hiroi, Appl. Phys. Lett. **79**, 2791 (2001)
51. A.D. Rae, J.G. Thompson, R.L. Withers, A.C. Willis, Acta Crystallogr. **B46**, 474–487 (1990)
52. C.H. Hervoches, P. Lightfoot, J. Solid State Chem. **153**, 66–73 (2000)
53. M.-W. Chu, M.T. Caldes, Y. Piffard, A.-M. Marie, E. Gautier, O. Joubert. J. Solid State Chem. **172**, 389–395 (2003)
54. K. Momma, F. Izumi, VESTA 3 for three-dimensional visualization of crystal, volumetric and morphology data. J. Appl. Crystallogr. **44**, 1272 (2011)
55. M. Osada, M. Tada, M. Kakihana, T. Watanabe, H. Funakubo, Jpn. J. Appl. Phys. **40**, 5572–5575 (2001)
56. I.D. Brown, Chem. Rev. **109**, 6858–6919 (2009)
57. N.A. Benedek, J.M. Rondinelli, H. Djani, P. Ghosez, P. Lightfoot, Dalton Trans. **44**, 10543–10558 (2015)
58. M.I. Aroyo, A. Kirov, C. Capillas, J.M. Perez-Mato, H. Wondratschek, Acta Crystallogr. Sect. A 62, 115 (2006)
59. J.M. Perez-Mato, D. Orobengoa, I.M. Aroyo Mode crystallography of distorted structures. Acta Crystallogr. **A66**, 558–590 (2010)
60. J.M. Perez-Mato, P. Blaha, K. Schwarz, M. Aroyo, D. Orobengoa, I. Etxebarria, A. Garcıa, Phys. Rev. B **77**, 184104 (2008)
61. Q. Zhou, B.J. Kennedy, C.J. Howard, Chem. Mater. **15**, 5025–5028 (2003)
62. X. Chen, C. Wei, J. Xiao, Y. Xue, X. Zeng, F. Yang, P. Li, Y. He, J. Phys. D **46**, 425001 (2013)
63. X.Q. Chen, F.J. Yang, W.Q. Cao, H. Wang, C.P. Yang, D.Y. Wang, K. Chen, Solid State Commun. **150**, 1221–1224 (2010)
64. J. Chen, Z. Tang, Y. Bai, S. Zhao J. Alloys Compds. **675**, 257–265 (2016)
65. D. Barrionuevo, S.P. Singh, M.S. Tomar, Integr. Ferroelectr. **124**, 41–47 (2011).
66. L. Pei, N. Hu, G. Deng, J. Sol-Gel Sci. Technol. **64**, 711–717 (2012)
67. L. Pei, M. Li, J. Liu, Mater. Lett. **64**, 364–366 (2010)
68. X.A. Mei, M. Chen, A.H. Cai, K.L. Su, C.Q. Huang, Z.M. Wan, Adv. Mater. Res. **105–106**, 259–262, (2010)
69. P. Zhou, Z. Mei, C. Yang, J. Mater. Sci. **27**, 7755–7759 (2016)
70. H. Qi, Y. Qi, M. Xiao, J. Mater. Sci. **25**, 1325 (2014)